AIP Journal of Applied Physics

Analytical modeling and numerical simulation of P+-Hg0.69 Cd0.31Te/n-Hg0.78Cd0.22Te/CdZnTe heterojunction photodetector for a long-wavelength infrared free space optical communication system

A. D. D. Dwivedi

Citation: J. Appl. Phys. **110**, 043101 (2011); doi: 10.1063/1.3615967
View online: http://dx.doi.org/10.1063/1.3615967
View Table of Contents: http://jap.aip.org/resource/1/JAPIAU/v110/i4
Published by the AIP Publishing LLC.

Analytical modeling and numerical simulation of P^+-$Hg_{0.69}Cd_{0.31}Te$/n-$Hg_{0.78}Cd_{0.22}Te$/CdZnTe heterojunction photodetector for a long-wavelength infrared free space optical communication system

A. D. D. Dwivedi[a)]
Centre for Applied Physics, Central University of Jharkhand, Brambe, Ranchi, Jharkhand 835205, India; Centre for Research in Microelectronics, Department of Electronics Engineering, IT-BHU, Varanasi, India

(Received 12 March 2011; accepted 24 June 2011; published online 16 August 2011)

In this paper an analytical modeling and 2D numerical simulation of P^+-$Hg_{0.69}Cd_{0.31}Te$/n-$Hg_{0.78}Cd_{0.22}Te$/CdZnTe single heterojunction photodetector using the commercially available ATLAS™ package from SILVACO® International for long-wavelength free space optical communication has been reported. The photodetector has been studied with respect to energy band diagram, electric field profile, doping profile, dark current, resistance area product, quantum efficiency, spectral response, responsivity, and detectivity by an analytical method using closed form equations. The results obtained on the basis of the analytical model have been compared and contrasted with the simulated results using ATLAS™. The photodetector exhibits high values of quantum efficiency ~80%, responsivity ~6.75 A/W, specific detectivity $\sim 2.25 \times 10^{11}$ $mHz^{1/2}W^{-1}$ at wavelength10.6 μm, and dark current of the order of 10^{-11} A. The estimated noise equivalent power (NEP) is of the order of 1×10^{-17} W. © *2011 American Institute of Physics*.
[doi:10.1063/1.3615967]

INTRODUCTION

Free space optical communication has drawn considerable attention because of its potential to serve applications requiring high bandwidth with relatively high security to eavesdropping but without the complexity of installing optical fibers. The basic advantages of free space optical communication systems include extremely high bandwidth, rapid deployment time, license and tariff free bandwidth allocation, low power consumption, light weight, small size, low loss, and no requirement of material medium through which information can be processed. It has been established that the long-wavelength infrared (LWIR) region is best suited for free space optical communication.[1] There are two strategic atmospheric windows in the LWIR region at 9.6 μm and 10.6 μm, which have drawn considerable research interest for development of free space optical communication systems. The strategic atmospheric window at 10.6 μm is more immune to adverse weather conditions, e.g., fog and haze. The beams, containing billions of bits of information comprising a combination of Internet messages, video images, radio signals, computer files, and so on, in free space optical (FSO) systems are transmitted by a laser source focused on highly sensitive ultrafast photodetectors as receivers. Such ultrafast high sensitivity receivers operating in the LWIR region deploy photovoltaic detectors based on narrow bandgap semiconductors. Using telescopic lenses, light is focused on receivers for collection of the photon stream and transmission of digital data. A number of photodetectors based on narrow bandgap semiconductors have been developed by several research groups over the past decades (Refs. 2–20 and references therein). The most promising semiconductor alloy for use in the LWIR region is HgCdTe (MCT) belonging to the II-VI family. Since the systematic cost of experimental investigations of $Hg_{1-x}Cd_xTe$ (MCT)-based photodetectors is very high, modeling and numerical simulation became critical tools for development of infrared photodetectors, as reported by many researchers in the recent past (Refs. 2–20 and references therein). Modeling and simulation work in the area of MCT-based photodetectors for development of design guidelines for device prototypes are very powerful tools. Therefore this paper presents an analytically developed model of a long-wavelength infrared (LWIR) photodetector based on $Hg_{1-x}Cd_xTe$ (MCT). Computations have been carried out on the basis of the developed model for a P^+-$Hg_{0.69}Cd_{0.31}Te$/n-$Hg_{0.78}Cd_{0.22}Te$/CdZnTe single heterojunction photodetector to explore the potential of the device for possible free space optical communication applications at 10.6 μm. The long-wavelength photodetector has been supposed to be grown on lattice matched CdZnTe substrate because interface trap charges are less for the HgCdTe/CdZnTe interface as compared to other substrates, e.g., Si, Ge, and CdTe. Recently, p-n junction heterostructures have shown extensive possibilities to improve the performance of existing IR detectors, exploiting the two strategic atmospheric transmission windows in the LWIR region (8–12 μm) (Refs. 2–20) at 9.6 μm and 10.6 μm. The basic advantages of a heterostructure photodetector are low power dissipation, low noise, faster response time, and potential for a more uniform spatial distribution for minority carrier transportation. In comparison to heterojunction photodetectors, homojunction photodetectors have a lower breakdown voltage, produce large reverse leakage current for high speed operation and suffer from low quantum

[a)]Present address: Department of Physics, School of Physical Sciences, Central University of Rajasthan, Rajasthan, India. Electronic address: adddwivedi@gmail.com and itbhu.arun@gmail.com.

efficiency.[19] In the present work, the single heterostructure P^+-$Hg_{0.69}Cd_{0.31}Te$/n-$Hg_{0.78}Cd_{0.22}Te$/CdZnTe photodetector has been simulated for applications in free space optical communication in LWIR (8–12 μm) region at 77 K. The simulation takes into account all forms of recombination processes including surface recombination.[20] The heterojunction photodetector is virtually grown on CdZnTe substrate using the SILVACO® ATHENA platform. The light is incident from the P^+-$Hg_{0.69}Cd_{0.31}Te$ side, which acts as window. The lightly doped n-type $Hg_{0.78}Cd_{0.22}Te$ material acts as the active layer of the heterojunction. The lightly doped narrow bandgap n-$Hg_{0.78}Cd_{0.22}Te$ absorbing region determines the dark current and photocurrent. The device has been simulated in terms of its electrical and optical characteristics. For electrical characterization we simulated the device with respect to its energy band diagram, electric field profile doping profile, dark current, and resistance area product, and for optical characterization the device has been simulated in terms of its spectral response, quantum efficiency, responsivity, and detectivity. For this purpose closed form expressions for diffusion current in dark and illuminated conditions and for quantum efficiency have been derived by solving diffusion equations using appropriate boundary conditions. Results obtained from the closed form expressions have been compared and contrasted from those obtained from the ATLAS™ simulation.

FORMULATION OF THE MODEL

The structure under consideration is a P^+-$Hg_{0.69}Cd_{0.31}Te$/n-$Hg_{0.78}Cd_{0.22}Te$/CdZnTe single heterojunction photodetector as shown in Fig. 1; its equilibrium condition energy band diagram is shown in Fig. 2. In the analysis, the incident light is assumed to be incident from the top P^+-$Hg_{0.69}Cd_{0.31}Te$ layer which acts as a cladding over the active n-$Hg_{0.78}Cd_{0.22}Te$ layer. The energy band diagram of a heterojunction photodetector can be obtained by applying the classical theory of Anderson (as cited by Sharma and Purohit).[21] According to Anderson's model the proposed P^+-$Hg_{0.69}Cd_{0.31}Te$/n-$Hg_{0.78}Cd_{0.22}Te$ heterojunction system forms a staggered type II B band alignment. However, Anderson's model is based on a number of simple and drastic assumptions, which are not true for practical heterojunctions. The analysis shows that there is energy offset in the conduction band ΔE_C and valance band ΔE_V, due to electron affinity differences. The formation of a potential barrier within the heterojunction can be understood in terms of forces that arise due to gradients in electrostatic potential ∇V and electron affinity $\nabla\chi$. The electrons will be dominated current carriers because the barrier is smaller for electrons as compared with holes. The drop in energy band at the p-n heterojunction shows the potential variation at the interface of the junction. The height of the potential barrier at the p-n heterojunction depends on the doping profile of the material.

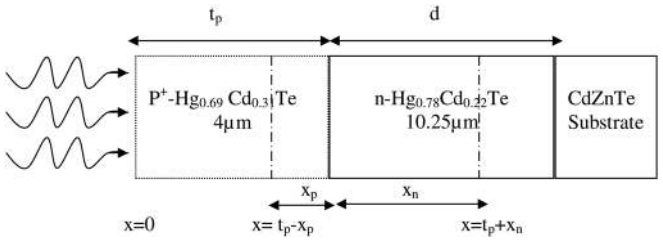

FIG. 1. The proposed device structure of P^+-$Hg_{0.69}Cd_{0.31}Te$/n-$Hg_{0.78}Cd_{0.22}Te$/CdZnTe LWIR P^+-n heterojunction photodetector.

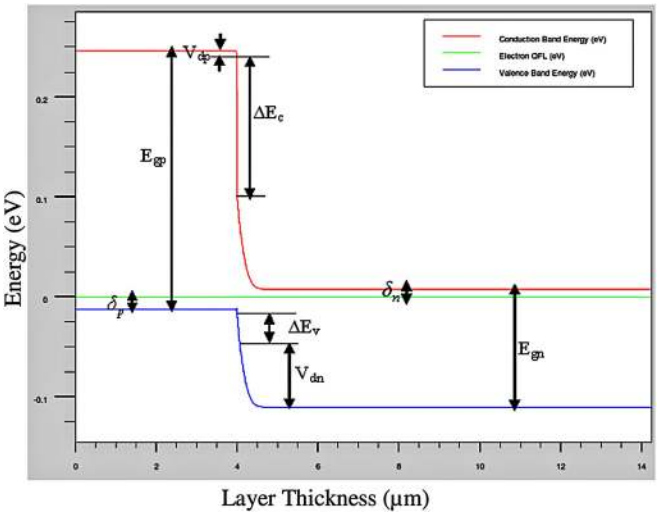

FIG. 2. (Color online) Equilibrium condition energy band diagram.

The energy bandgaps of the two semiconductors, their conduction and valance band-edge discontinuities (which are dependent on E_{gn}, E_{gp}, N_A, N_D, χ, and the location of the p-n junction) and the built-in potential V_d after formation of the heterojunction are interrelated, as follows:[21]

$$V_d = V_{dp} + V_{dn}, \tag{1}$$

$$\Delta E_g = \Delta E_C + \Delta E_V, \tag{2}$$

$$\Delta E_C = \chi_n - \chi_p, \tag{3}$$

$$\Delta E_g = E_{gp} - E_{gn}, \tag{4}$$

$$E_{gp} = \delta_p + \delta_n - V_d + \Delta E_C, \tag{5}$$

$$\Delta Q_C = \frac{\Delta E_C}{\Delta E_g}, \tag{6}$$

$$\Delta Q_V = \frac{\Delta E_V}{\Delta E_g}, \tag{7}$$

($E_{gp} = 0.2582$ eV, $E_{gn} = 0.1170$ eV, $\Delta E_g = E_{gp} - E_{gn} = 0.1412$ eV, $\Delta E_C = \chi_n - \chi_p = 0.1147$ eV, $\Delta E_V = 0.0265$ eV).

Here, V_d is the total built-in potential, ΔE_g is the total band-edge discontinuity; and ΔE_C and ΔE_V are the conduction and valence band-edge discontinuities at the heterointerface, respectively. Here χ_p and χ_n are the electron affinities of the wide and narrow bandgap materials, respectively; and E_{gp} and E_{gn} are the corresponding energy bandgaps. δ_p and δ_n are the separations between the Fermi level and band-edges (valence band-edge in the case of p-type and conduction band-edge in the case of n-type material) in the n and p regions, respectively. V_{dn} and V_{dp} are the barriers corresponding to band bending on the n- and p sides. Q_C and Q_V are the fractional band offsets for the conduction and valence bands of the materials, respectively.

The incident light enters through the larger energy bandgap P^+-$Hg_{0.69}Cd_{0.31}Te$ cladding layer that acts as window. The incident light is absorbed in the lightly doped n-$Hg_{0.78}Cd_{0.22}Te$ layer, which acts as an active region. All photogenerated carriers in the depletion region as well as those generated in the neutral P^+ and n region within their respective diffusion lengths from the edges of the depletion region will cross the junction and contribute to the total photocurrent. The performance of the photodetector is greatly influenced by the total dark current arising from the thermally generated carriers. The total dark current of the detector under consideration constitutes the contribution of the following current components (i) the diffusion of the thermally generated carriers in the neutral region, I_{DIFF}; (ii) generation recombination of carriers in the depletion region, I_{GR}; and (iii) tunneling of the carriers across the heterojunction, I_{TUN}. The tunneling current arises from the contribution of both band to band (BTB) tunneling, and tunneling via defect levels in the bandgap of the material. The latter component is generally known as trap-assisted tunneling (TAT).

The total dark current density is the sum of all three components and can be written as

$$J_{Total} = J_{DIF} + J_{GR} + J_{TUN}, \tag{8}$$

where $J_{TUN} = J_{BTB} + J_{TAT}$.

The subscripts represent the mechanism responsible for the corresponding current components (i.e., Diffusion, G-R, BTB, or TAT).

Diffusion component

The fundamental current component in photovoltaic detectors is the diffusion current arising from the minority carriers extracted from the P^+-$Hg_{0.69}Cd_{0.31}Te$ and n-$Hg_{0.78}Cd_{0.22}Te$ regions. In order to model the diffusion component of current in LWIR photodetectors it is necessary to estimate the effective lifetime of the extracted carriers. There are three mechanisms of carrier recombination in the device under consideration. These are as follows: (i) Schockley-Read-Hall (SRH) process via lattice defect and impurity level within the forbidden gap, (ii) radiative process arising out of direct BTB transition, and (iii) non-radiative Auger recombination, a three state transition process. Among these three processes, the first (SRH) can be easily controlled by improving the fabrication procedure. The other two mechanisms are prevalent in photovoltaic detectors made of narrow bandgap (direct) semiconductors. The Auger process becomes more dominant as the temperature increases and becomes crucial at or near room temperature. It is understood that Auger mechanism is most likely to impose the fundamental limit to the performance of photovoltaic detectors, based on narrow bandgap materials.[19] Taking into account all three dominant recombination processes, e.g., Auger, radiative, and SRH recombination mechanisms for computation of minority carrier lifetime, the effective lifetime of the carriers in the active region can be evaluated as

$$\frac{1}{\tau} = \frac{1}{\tau_{SRH}} + \frac{1}{\tau_R} + \frac{1}{\tau_{Aug}}, \tag{9}$$

where τ_{Aug} corresponds to the overall value of the mean lifetime of the carriers due to Auger recombination. The band to band Auger effects are classified in several processes according to related bands. Beattie has determined 10 types of photon-less Auger recombination mechanisms that are possible in a semiconductor with a single conduction band and heavy and light hole valence bands.[20] They have the smallest threshold ($E_T \approx E_g$) and the largest combined density of states. The CHCC recombination mechanism (Auger-1) involves two electrons and a heavy hole and is dominant in n-type material. The CHLH process (Auger-7) is dominant in p-type material if the spin split-off band can be ignored. For materials such as $Hg_{1-x}Cd_xTe$, where the spin split-off energy Δ is much larger than the bandgap energy E_g, the probability of the Auger transition through the conduction band/heavy-hole band/spin split-off band mechanism (called CHSH or Auger S) may be negligibly small in comparison with that of the CHLH Auger transition. Hence for narrow gap $Hg_{1-x}Cd_xTe$ only Auger-1 and Auger-7 need to be considered. The Auger lifetime (τ_{Aug}) is expressed as

$$\frac{1}{\tau_{Aug}} = \frac{1}{\tau_{A1}} + \frac{1}{\tau_{A7}}, \tag{10}$$

where τ_{A1} and τ_{A7} are lifetimes of carriers due to Auger-1 and Auger-7 transitions, respectively.[3] The radiative process takes place when free electrons and holes recombine, emitting the excess energy in the form of a photon. The recombination rate for bands with spherical symmetry depends on the absorption coefficient through the equation[20]

$$G_R = \frac{8\pi}{h^3 c^3} \int_0^\infty \frac{\varepsilon(E)\alpha(E)E^2 dE}{\exp(E/kT) - 1}, \tag{11}$$

where $\alpha(E)$ is the optical absorption coefficient, $\varepsilon(E)$ is the relative dielectric constant, h is Planck's constant and c is the speed of light. Ignoring the dispersion in dielectric constant and using the high frequency value of the dielectric constant the radiative lifetime can be obtained as[20]

$$\tau_R = \frac{n_i^2}{G_R(n_0 + p_0)}, \tag{12}$$

where n_i is intrinsic carrier concentration, and n_0 and p_0 are the thermal equilibrium concentrations for electrons and holes, respectively. The dependence of α on E as analyzed by Bardeen *et al*. can be expressed as[22]

$$\alpha(E) = \frac{2^{2/3} m_0 q^2}{3\varepsilon_\infty^{1/2}\hbar^2} \left(\frac{m_n^* m_h^*}{m_0(m_n^* + m_h^*)}\right)^{3/2} \times \left(1 + \frac{m_0}{m_n^*} + \frac{m_0}{m_h^*}\right)\left(\frac{E - E_g}{m_0 c^2}\right)^{1/2}, \tag{13}$$

where E_g is the material bandgap, m_0 is free electron mass, m_n^* is the effective mass of electrons, m_h^* is the effective mass of holes, ε_∞ is the high frequency dielectric constant, E_g is the material bandgap in eV, and $\hbar = h/2\pi$, h being Planck's constant. On the basis of this expression, assuming $E_g > kT$

and neglecting the dispersion in the dielectric, we can obtain G_R as[20]

$$G_R = 5.8 \times 10^{-13} n_i^2 \varepsilon_\infty^{1/2} \left(1 + \frac{m_0}{m_n^*}\right) \left(\frac{m_0}{m_n^* + m_h^*}\right)^{3/2} \times \left(\frac{300}{T}\right)^{3/2} \left(E_g^2 + 3kTE_g + 3.75k^2T^2\right), \quad (14)$$

where k is Boltzmann's constant, T is temperature, and n_i is the intrinsic carrier concentration. The Shockley-Read Hall mechanism is not an intrinsic process, as it occurs via levels in the forbidden energy gap. It may be reduced by lowering concentrations of native defects and foreign impurities. In the Shockley-Read Hall mechanism, generation and recombination occurs via energy levels introduced by impurities or lattice defects into the forbidden energy gap. As recombination centers they trap electrons and holes; as generation centers, they successively emit them. The rates of generation and recombination depend on the individual nature of the center and its predominant occupation state of the charge carriers as well as on the local densities of those carriers in the bands of the semiconductor.

The lifetime of carriers due to Schockley-Read Hall (SRH) recombination can be modeled in terms of trap density and capture cross-section as[23]

$$\tau_{SRH} = \frac{1}{\sigma N_f v_{th}}, \quad (15)$$

where N_f is the SRH trap density, σ is the capture cross-section of minority carriers, and v_{th} is the thermal velocity of the minority carriers in the active region, given by

$$v_{th} = \sqrt{\frac{3kT}{m_h^*}}. \quad (16)$$

The standard one-dimensional diffusion equation for the heterojunction (type II B) under consideration has been solved analytically under appropriate boundary conditions to obtain the expression for the diffusion components of current density in the neutral P^+ and n regions. The diffusion component of current density for electrons and holes can be obtained as[24]

$$J_{sn} = \frac{qn_{ip}^2}{N_A} \sqrt{\frac{\mu_n kT}{q\tau_n}} \frac{\frac{S_n L_n}{D_n} \cosh\left(\frac{t_p - x_p}{L_n}\right) + \sinh\left(\frac{t_p - x_p}{L_n}\right)}{\frac{S_n L_n}{D_n} \sinh\left(\frac{t_p - x_p}{L_n}\right) + \cosh\left(\frac{t_p - x_p}{L_n}\right)} \times \exp\left(\frac{-q(V_d + \Delta E_c)}{kT}\right), \quad (17)$$

$$J_{sp} = \frac{qn_{in}^2}{N_D} \sqrt{\frac{\mu_h kT}{q\tau_h}} \frac{\frac{S_p L_p}{D_p} \cosh\left(\frac{d - x_n}{L_p}\right) + \sinh\left(\frac{d - x_n}{L_p}\right)}{\frac{S_p L_p}{D_p} \sinh\left(\frac{d - x_n}{L_p}\right) + \cosh\left(\frac{d - x_n}{L_p}\right)} \times \exp\left(\frac{-q(V_d + \Delta E_v)}{kT}\right). \quad (18)$$

In the above equations, n_{in} and n_{ip} are the intrinsic carrier concentrations of HgCdTe in n and p regions; N_A and N_D are the acceptor and donor concentrations in the p and n regions, respectively; q is the electronic charge; μ_h and $\mu_n$are the hole and electron mobilities, respectively; τ_h and τ_n are the hole and electron lifetimes, respectively; S_p and S_n are the surface recombination velocities of holes and electrons at the heterointerface; and L_p and L_n are the diffusion lengths of holes and electrons on n and p sides, respectively. Here t_p and d are the thickness of P^+-HgCdTe cladding layer and n-HgCdTe active regions, respectively; x_p and x_n are the width of the depletion regions in p and n regions, respectively; and V_d is the total barrier voltage at the heterointerface. The total diffusion current density can be obtained as

$$J_{DIFF} = (J_{sn} + J_{sp}) \left(\exp\left(\frac{qV}{kT}\right) - 1\right). \quad (19)$$

G-R component

The carriers generated in the depletion region are generally separated out under the action of the existing electric field. These carriers contribute to the total current flowing through the detector. The transport of carriers across the heterojunction under consideration is strongly affected by the trap levels at the heterointerface inside the depletion region. The current component arising from the G-R in the depletion region can be obtained as[24]

$$J_{GR} = 2\sqrt{3(kT)^3}\sigma N_f \left[\frac{n_{in} x_n}{V_{dn}} \sqrt{\frac{1}{m_{nn}^*}} + \frac{n_{ip} x_p}{V_{dp}} \sqrt{\frac{1}{m_{pp}^*}}\right] \exp\left(\frac{qV}{2kT}\right), \quad (20)$$

where m_{nn}^* and m_{pp}^* are the effective masses of electrons and holes in the n and P^+ regions, respectively.

Tunneling mechanism

In the present heterojunction photodetector electrons and holes are separated by the depletion region at the heterointerface. Under applied reverse bias the holes from P^+ region will tunnel through the barrier on the n side. The tunneling may occur (a) via defect levels in the bandgap of the material, generally known as trap assisted tunneling (TAT), or from band-to-band (BTB).

Trap assisted tunneling

In this case the minority carriers may tunnel from the occupied trap states on the quasi neutral side to the empty band states on the other side of the junction or through the trap sites present in the depletion region of the junction. In the P^+-n junctions, the major contribution of TAT may be due to tunneling of electrons, via trap levels to the conduction band on the n side. This trap-assisted tunneling current density can be calculated as[17]

$$J_{TAT} = \frac{q^3 \pi^2 m_p x_w E M^2 N_t}{\hbar^3 (E_g - E_t)} \exp\left(-\frac{8\pi \left(2m_{pp}^*\right)^{\frac{1}{2}} (E_g - E_t)^{\frac{3}{2}}}{3q\hbar E}\right), \quad (21)$$

where x_w is the total width of the depletion region, m^*_{pp} is the effective mass of holes in the valence band, M is the matrix element associated with the trap potential, E is the electric field across the depletion region, and N_t is the trap density responsible for trap assisted tunneling, which is different from the SRH trap density. E_t is the position of the trap levels in the bandgap measured from the top of the valence band.

Band to band tunneling

At relatively higher bias voltage, the electrons from the filled in states in the valence band on the P^+ side tunnel to the conduction band on the n side. This band to band current density can be obtained as[25,26]

$$J_{BTB} = \frac{q^3 EV}{4\pi^2\hbar^2}\sqrt{\frac{2m^*_{pp}}{E_g}}\exp\left(-\frac{4\sqrt{2m^*_{pp}E_g^3}}{3q\hbar E}\right), \quad (22)$$

Here, V is the applied voltage, m^*_{pp} is the effective mass of holes in the valence band, E is the electric field across the depletion region, and $\hbar = h/2\pi$, h being Planck's constant.

The resistance area product for the individual components (DIF, GR, and TUN, TAT and BTB) can be obtained as

$$(RA)_x = \left(\frac{dJ_x}{dV}\right)^{-1}, \quad (23)$$

where the superscript x corresponds to different components. The net or effective value of the resistance area product $(RA)_{\mathrm{NET}}$ is given by

$$\frac{1}{(RA)_{NET}} = \frac{1}{(RA)_{DIFF}} + \frac{1}{(RA)_{GR}} + \frac{1}{(RA)_{TAT}} + \frac{1}{(RA)_{BTB}}. \quad (24)$$

Quantum efficiency

The quantum efficiency (η) of a P^+-n heterojunction photodetector has three major components. These components arise from the contribution of the three regions, e.g., neutral n-region (η_n), neutral p-region (η_p), and the depletion region (η_{dep}). The optical generation rate of electron-hole pairs, as a function of distance x from the surface can be written as[27–30]

$$G_p(x) = \frac{\alpha_p(\lambda)(1-R_p)P_{opt}}{Ah\nu}\exp(-\alpha_p(\lambda)x), \quad (25)$$

$$G_n(x) = \frac{\alpha_n(\lambda)(1-R_p)(1-R_n)P_{opt}}{Ah\nu}\exp(-\alpha_n(\lambda)x), \quad (26)$$

where $\alpha(\lambda)$ is the optical absorption coefficient of the material, which is a function of wavelength λ; R_n and R_p are the Fresnel reflection coefficients at the computing interfaces; P_{opt} is the incident optical power; ν is the frequency of radiation; and A is the device area. The quantum efficiency components can be obtained as[27–30]

$$\eta_p = \frac{(1-R_p)\alpha_p L_n}{\alpha_p^2 L_n^2 - 1}\left[\frac{\alpha_p L_n + \gamma_n - \exp(-\alpha_p(t_p - x_p))\left[\gamma_n \cosh\left(\frac{t_p - x_p}{L_n}\right) + \sinh\left(\frac{t_p - x_p}{L_n}\right)\right]}{\gamma_n \sinh\left(\frac{t_p - x_p}{L_n}\right) + \cosh\left(\frac{t_p - x_p}{L_n}\right)} - \alpha_p L_n \exp(-\alpha_p(t_p - x_p))\right], \quad (27)$$

$$\eta_n = \frac{(1-R_n)(1-R_p)\alpha_n L_p}{\alpha_n^2 L_p^2 - 1}\exp(-(\alpha_p t_p + \alpha_n x_n))\left[\frac{(\gamma_p - \alpha_n L_p)\exp(-\alpha_n(d - x_n)) - \left[\gamma_p \cosh\left(\frac{d - x_n}{L_p}\right) + \sinh\left(\frac{d - x_n}{L_p}\right)\right]}{\gamma_p \sinh\left(\frac{d - x_n}{L_p}\right) + \cosh\left(\frac{d - x_n}{L_p}\right)} + \alpha_n L_p\right], \quad (28)$$

where L_p and L_n are the hole and electron diffusion lengths in n and p regions, respectively, and $\gamma_n = S_n L_n/D_n$ and $\gamma_p = S_p L_p/D_p$ are the ratio of surface to bulk recombination velocities in n and p regions, respectively.

The contribution of the photo-generated carriers in the depletion region to the total quantum efficiency can be obtained as

$$\eta_{dep} = (1-R_n)(1-R_p)\{\exp(-\alpha_p(t_p - x_p)) - \exp(-\alpha_n(t_p + x_n))\}. \quad (29)$$

The net quantum efficiency can be written as

$$\eta = \eta_n + \eta_p + \eta_{dep}. \quad (30)$$

Specific detectivity

The most important figure of merit of the photodetector for use in optical communication is the specific detectivity D^*, which depends on the wavelength of incident light λ, the quantum efficiency η, and the zero bias resistance area product, R_0A. As the dark current of the detector is contributed by three major components, i.e., diffusion, generation-

recombination, and tunneling (which includes trap assisted tunneling (TAT) and band to band tunneling (BTB)), the detectivity of the photodetector under consideration should be estimated from the net value of the R_0A product arising out of these mechanisms. The specific detectivity of the photodetector, which is a function of the applied voltage, can be written as

$$D^* = \frac{q\eta\lambda}{hc}\sqrt{\frac{(R_0A)_{NET}}{4kT}}. \tag{31}$$

Responsivity

The current responsivity (R) of the photodetector is given as

$$\mathrm{R} = \frac{\eta q\lambda}{hc}. \tag{32}$$

Noise equivalent power

The variation of noise equivalent power (NEP) with wavelength can be written as

$$NEP = \frac{A^{1/2}B^{1/2}}{D^*}, \tag{33}$$

where A is the area of the detector and B is the bandwidth; here NEP is calculated at unity bandwidth ($B = 1$ Hz).

RESULTS AND DISCUSSION

The proposed device structure is shown in Fig. 1. It consists of highly doped P^+-$Hg_{0.69}Cd_{0.31}Te$ over lightly doped n-$Hg_{0.78}Cd_{0.22}Te$, which is virtually grown on a suitable substrate such as CdZnTe or sapphire using the ATHENA tool of ATLAS™, device simulation software from SILVACO® International. The light has been assumed to be incident on the top P^+-$Hg_{0.69}Cd_{0.31}Te$ side of the photodetector. The incident light is absorbed in n-$Hg_{0.78}Cd_{0.22}Te$ regions. The operation performance of the HgCdTe-based P^+n photodetector has been studied using a two-dimensional, drift-diffusion approach using a commercial numerical device simulator, ATLAS™. The HgCdTe-based P^+-n heterojunction photodiode for long-wavelength free space optical communications has been proposed. The numerical simulation of a P^+-n photodetector has been carried out for a non-degenerate semiconductor and parabolic conduction band. The simulation involves solution of five coupled equations using Newton's iteration technique. The doping of the regions has been taken as analytically uniform for all regions in the above simulation. In calculation of mobility the concentration-dependent ANALYTIC model has been considered. For the simulation of dark current, associated with the P^+-n photodetector, AUGER, CONSRH, and OPTICAL (band-to-band) models have been taken into account for recombination mechanism modeling. The band-to-band standard tunneling model has been considered for the tunneling mechanism. The surface recombination process at the heterointerface and at metal contacts has been taken into account in the simulation and also in the analytical model. The quality of the interface has been characterized in terms of surface recombination velocity. We have taken into account the Fermi-Dirac statistics for the parabolic shape of the conduction band in all the calculations of carrier and doping densities. For the simulation of dark current associated with P^+-n heterojunction photodetector, the optical, SRH, Auger, and surface recombination rates are given as:[3]

$$R_{np}^{OPT} = C_c^{OPT}\left(pn - n_i^2\right), \tag{34}$$

$$R_{SRH} = \frac{pn - n_i^2}{\left[\tau_{p0}\{n + n_i\exp(E_t/kT)\} + \tau_{n0}\{p + n_i\exp(-E_t/kT)\}\right]}, \tag{35}$$

$$R_{Aug} = C_n\left(pn^2 - nn_i^2\right) + C_p\left(p^2n - pn_i^2\right), \tag{36}$$

$$R_{Surf} = \frac{pn - n_i^2}{\left[\tau_p^{eff}\{n + n_i\exp(E_t/kT)\} + \tau_n^{eff}\{p + n_i\exp(-E_t/kT)\}\right]}, \tag{37}$$

Here C_c^{OPT} is the capture rate of carriers and C_n and C_p are and Auger coefficients for electrons and holes, respectively. Here n and p are equilibrium electron and hole concentration; E_t is the energy level of the trap; n_i is the intrinsic carrier concentration; τ_{p0} and τ_{n0} are the SRH lifetimes of holes and electrons, respectively; and τ_p^{eff} and τ_n^{eff} are effective lifetimes of holes and electrons, respectively.

Numerical computations have been carried out on P^+-$Hg_{0.69}Cd_{0.31}Te$/n-$Hg_{0.78}Cd_{0.22}Te$/CdZnTe LWIR P^+-n heterojunction photodetectors at 77 K for operation at 10.6 μm. The light has been assumed to be incident on the top P^+-$Hg_{0.69}Cd_{0.31}Te$ side of the photodetector. The photons with energy higher than the energy gap create electron-hole pairs in the n region. The mole fraction of cadmium in the ternary MCT material has been calculated so that the bandgap energy of the material corresponds to the long wavelength cut-off value of 10.6 μm for LWIR free space optical communication. The bandgap of $Hg_{1-x}Cd_xTe$ as a function of temperature, T, and alloy composition, x, is included in the simulation model using the following empirical formula:[20]

$$E_g = -0.302 + 1.93x - 0.810x^2 + 0.832x^3 + 5.35\times10^{-4}(1-2x)\left(\frac{-1822 + T^3}{255.2 + T^2}\right). \tag{38}$$

The intrinsic carrier concentration was calculated using the following expression:[31]

$$n_i = (5.24256 - 3.57290x - 4.74019\times10^{-4}T + 1.25942\times10^{-2}xT - 5.77046x^2 - 4.24123\times10^{-6}T^2)\times10^{14}E_g^{3/4}T^{3/2}\exp\left(\frac{-E_g}{2kT}\right), \tag{39}$$

where k is Boltzmann's constant. From the Kane band model the hole effective mass is taken as $m_h^* = 0.55\ m_0$ and the electron effective mass has been computed following Ref. 32 as

$$\frac{m_0}{m_n^*} = 1 + 2F + \frac{E_p}{3}\left(\frac{2}{E_g} + \frac{1}{E_g + \Delta}\right) \tag{40}$$

where $E_p = 19$ eV, F $= -0.8$ and $\Delta = 1.0$ eV. The electron mobility has been computed using the empirical formula given by:[20]

$$\mu_n = \frac{9 \times 10^4 s}{T^{2r}} \mathrm{m^2/Vs}, \tag{41}$$

where $r = (0.2x)^{0.6}$ and $s = (0.2/x)^{7.5}$, which are valid in the composition range $0.2 \leq x \leq 0.6$ and temperature range T > 50 K.

The hole mobility has been assumed to be of the form[20]

$$\mu_n = \mu_0 \left[1 + \left(\frac{p}{1.8 \times 10^{23}}\right)^2\right]^{-1/4}, \tag{42}$$

where $\mu_0 = 0.044$ m^2/Vs.

The absorption coefficient of $Hg_{1-x}Cd_xTe$ for optical carrier generation can be calculated within the Kane model, including the Moss-Burstein shift. For photon energy $E < E_g$ (tail region), $\alpha < \alpha_g$, the absorption coefficient obeys the rule[33,34]

$$\alpha = \alpha_0 \exp\left(\frac{\delta(E - E_0)}{kT}\right), \tag{43}$$

and, for photon energy $E > E_g$(Kane region), the absorption coefficient obeys the rule

$$\alpha = \alpha_g \exp\left(\beta\left(E - E_g\right)\right)^{1/2}, \tag{44}$$

where α_0 is the fitting parameter and

$$E_0 = -0.355 + 1.77x, \tag{45}$$

$$\frac{\delta}{kT} = \frac{\ln \alpha_g - \ln \alpha_0}{E_g - E_0}, \tag{46}$$

$$\alpha_g = -65 + 1.88T + (8694 - 10.315T)x, \tag{47}$$

$$\beta = -1 + 0.083 + (21 - 0.13T)x. \tag{48}$$

TABLE I. Parameters used in the computation model.

Parameters	Values
E_g	$-0.302 + 1.93x - 0.810x^2 + 0.832x^3$ $+ 5.35 \times 10^{-4}(1 - 2x)\left(\frac{-1822 + T^3}{255.2 + T^2}\right)$eV
Δ	1 eV
N_T	2.1×10^{19} m^{-3}
S	4.7619×10^{-20} m^2
N_D	9×10^{20} m^{-3}
N_A	2×10^{23} m^{-3}
M^2	10^{-29} V^{2}m^3
S_p	10 m/s
S_n	10^3 m/s
χ	$4.23 - 0.813(E_g - 0.083)$ eV (Refs. 12 and 35)
N_c	3.793×10^{22} m^{-3}
N_v	5.1204×10^{24} m^{-3}
C_n	8.3×10^{-32} m^6/s
C_p	3.33×10^{-31} m^6/s
C_C^{OPT}	4.87×10^{-16} m^6/s

The expressions of the high-frequency dielectric constant ε_∞ and static dielectric constant ε_s are obtained as a function of x as[20]

$$\varepsilon_\infty = 15.2 - 15.6x + 8.2x^2, \tag{49}$$

$$\varepsilon_s = 20.5 - 15.6x + 5.7x^2. \tag{50}$$

The parameters used in the computation are listed in Table I.

The different components of the dark current and *RA* product have been calculated using the theoretical model discussed in the previous section. The variation of quantum efficiency, current responsivity, specific detectivity, and noise equivalent power (NEP) with wavelength at 77 K has been computed from the above mentioned model.

The proposed photodetector structure has also been simulated using device simulation software ATLAS™ from SILVACO® International. A program was developed separately for calculation of various characteristics of the photodetector using a MATLAB platform by choosing appropriate material parameters.

The simulated results were obtained by developing a program in a DECKBUILD window interfaced with ATLAS for P^+-$Hg_{0.69}Cd_{0.31}Te/n^0$-$Hg_{0.78}Cd_{0.22}Te$/CdZnTe, P^+-n heterojunction photodetector at 77 K. Instead of the graded doping the numerical model includes a uniform doping profile. Once the physical structure of the photodetector is built in ATLAS, the properties of the material used in the device must be defined. A minimum set of material properties data includes bandgap, dielectric constant, electron affinity, densities of conduction and valance band states, electron and hole mobility, optical recombination coefficient, and an optical file containing the wavelength-dependent refractive index n,[35–37] and the extinction coefficient K (Refs. 35–37) for the used materials. The wavelength-dependent values of the extinction coefficient K are computed from the relation[35–37]

$$K = \frac{\alpha\lambda}{4\pi}. \tag{51}$$

The energy band diagram has been simulated from BLAZE, which is interfaced with ATLAS and is a general purpose 2D device simulator for III-V and II-VI materials and devices with position-dependent band structure (i.e., heterojunctions).[35] BLAZE accounts for the effects of positionally dependent band structure by modifications to the charge transport equations. An equilibrium condition energy band diagram for electrons is shown in Fig. 2, which has been simulated using BLAZE. The equilibrium condition electric field profile of the photodetector is shown in Fig. 3. The equilibrium condition doping profile of the device is shown in Fig. 4 which also shows the position-dependent electron and hole concentrations inside the device in different regions.

The optical characteristics of the device have been studied by using the LUMINOUS tool of the ATLAS device simulator. Of primary importance to the simulation of the photodetector is the accurate modeling of electron hole pair generation. LUMINOUS, the optoelectronic simulation module in ATLAS, determines the photogeneration at each mesh point in an ATLAS structure by performing two simultaneous calculations. The

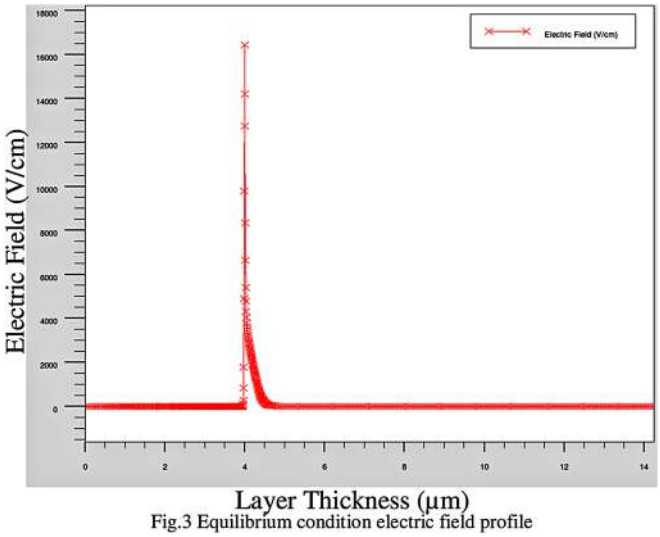

FIG. 3. (Color online) Equilibrium condition electric field profile.

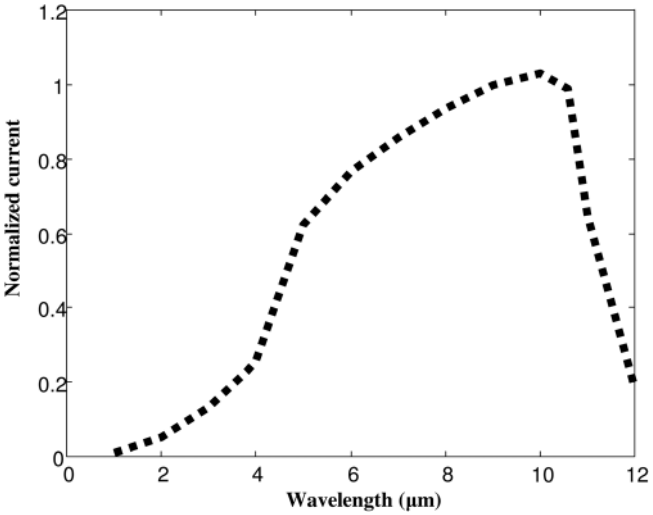

FIG. 5. Normalized spectral response.

refractive index n is used by LUMINOUS to perform an optical ray trace in the device. Differences in n values across the material boundaries determine the rate of light transmission and reflection. By following the path of light from the source to a mesh point, LUMINOUS is able to determine the optical intensity at that point. Together, these simulations provide for wavelength-dependent photogeneration throughout the photodetector.[35–37]

The normalized spectral response of the photodetector is shown in Fig. 5. It is a plot of normalized terminal current in case of illumination against wavelength of operation. Normalized current increases with wavelength of operation and attains a maximum value at $\lambda = 10.6$ μm and there is a sharp fall beyond $\lambda = 10.6$ μm which is the longer cutoff wavelength for the proposed composition of the $Hg_{1-x}Cd_xTe$, which is the absorbing layer in the proposed photodetector. The spectral response of the photodetector showing the variation of actual value of the cathode current, source photocurrent, and available photocurrent with wavelength is shown in

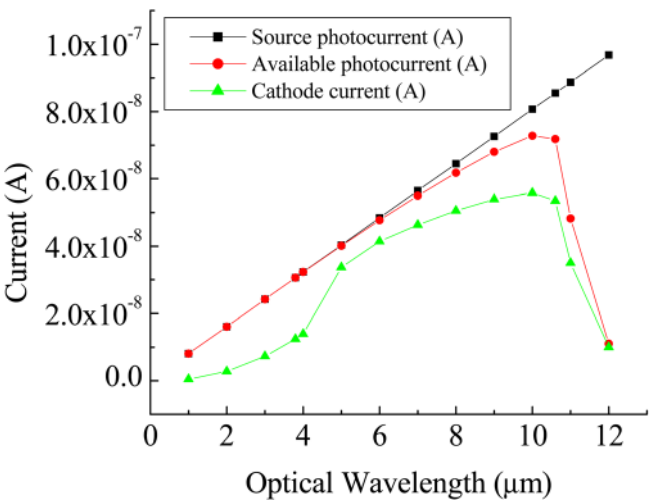

FIG. 6. (Color online) Spectral response of a heterojunction photodetector.

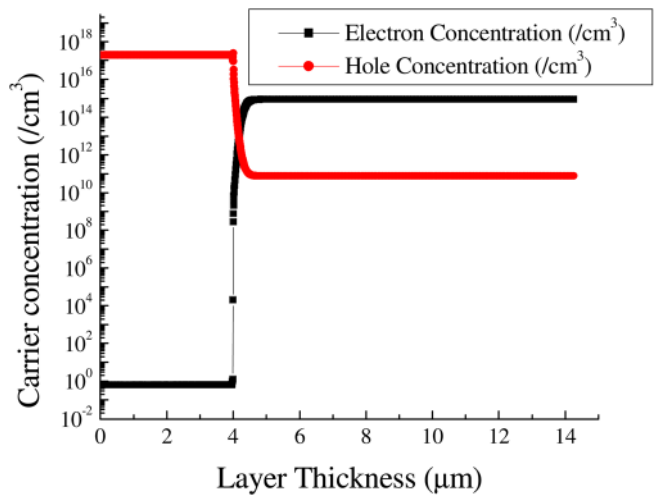

FIG. 4. (Color online) Equilibrium condition doping profile.

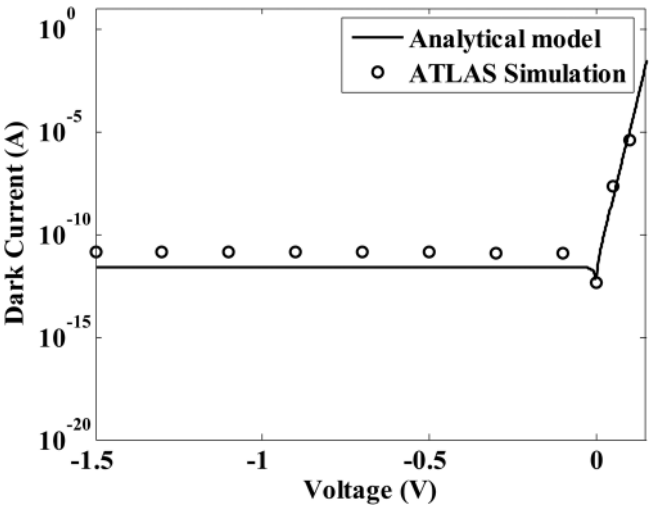

FIG. 7. Variation of dark current with voltage.

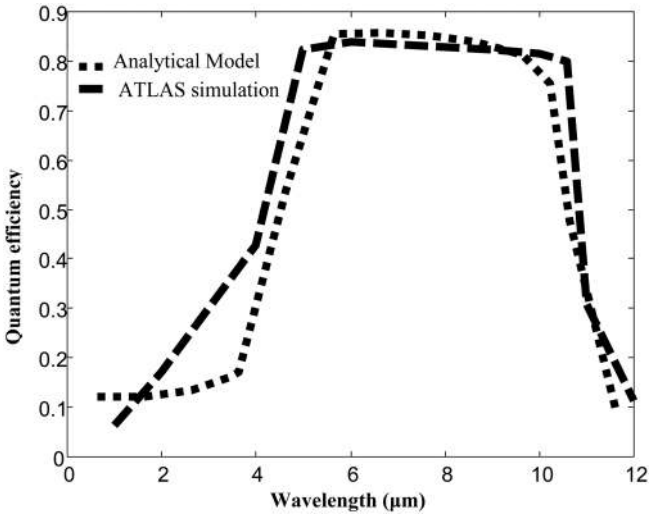

FIG. 8. Variation of quantum efficiency with wavelength.

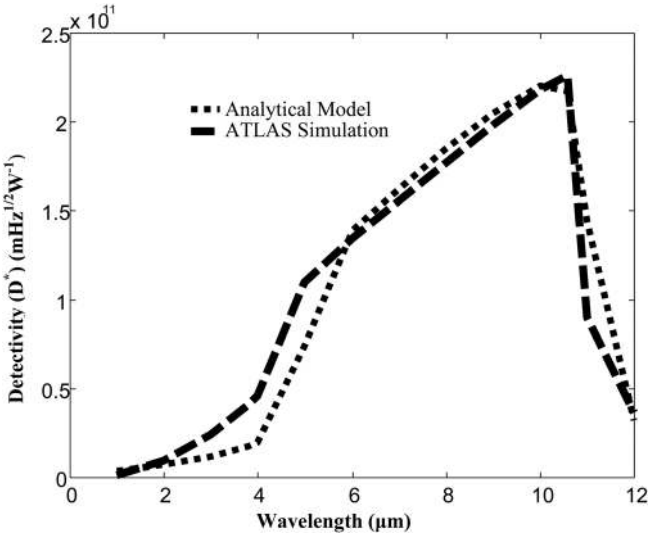

FIG. 10. Variation of detectivity (D^*) with wavelength.

Fig. 6. All the results discussed above have been obtained by ATLAS simulation.

Figure 7 shows variation of dark current with voltage as obtained from the analytical model and ATLAS simulation. It is clear from this figure that there is a good agreement between dark current obtained from the analytical model and that obtained from the ATLAS simulation, and the device exhibits very low dark current of the order of 10^{-11} A. Therefore it is very much suitable for low noise applications in free space optical communication at 10.6 μm. Variation of quantum efficiency of a P^+-n photodetector with wavelength of operation obtained from the analytical model and ATLAS simulation at a bias voltage of 0.5 V is shown in Fig. 8. From this figure it is clear that there is a good agreement between quantum efficiency obtained by the analytical model and that obtained by ATLAS simulation. The device exhibits very high quantum efficiency $\sim 80\%$, which attributes the high detectivity of the photodetector. This high quantum efficiency is obtained at the cost of bandwidth of the device because there is a tradeoff between quantum efficiency and 3 dB bandwidth. We can optimize the performance of the device by changing the doping concentration and dimensions of the device for high bandwidth performance but with lower quantum efficiency. The variation of responsivity of the photodetector with wavelength of operation is shown in Fig. 9. From this figure we can see that responsivity values obtained on the basis of the analytical model are close to those obtained from ATLAS simulation. The device exhibits very high values of responsivity, $\sim$6.75 A/W at wavelength 10.6 μm and a bias voltage of 0.5 V. Figure 10 shows variation of specific detectivity with wavelength of operation, which indicates that the order of detectivity values obtained by the analytical model and those obtained by ATLAS simulation are very close. The device exhibits very high values of specific detectivity, $\sim 2.25 \times 10^{11}$ $mHz^{1/2}W^{-1}$ at wavelength of operation 10.6 μm and a bias voltage of 0.5 V. Figure 11

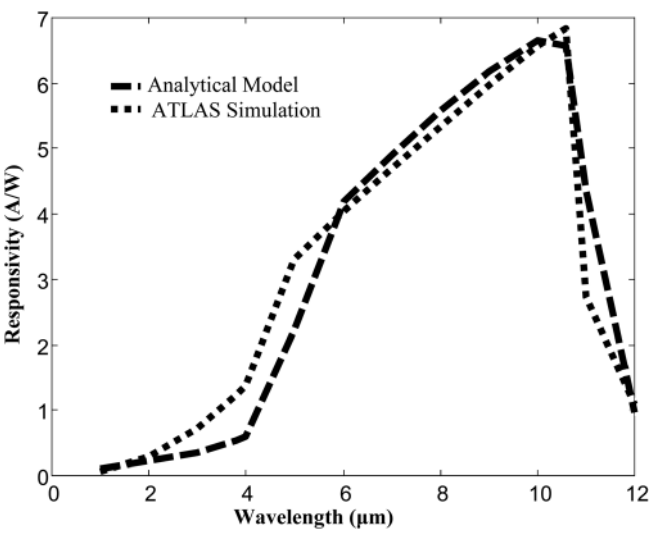

FIG. 9. Variation of responsivity of photodetector with wavelength of operation.

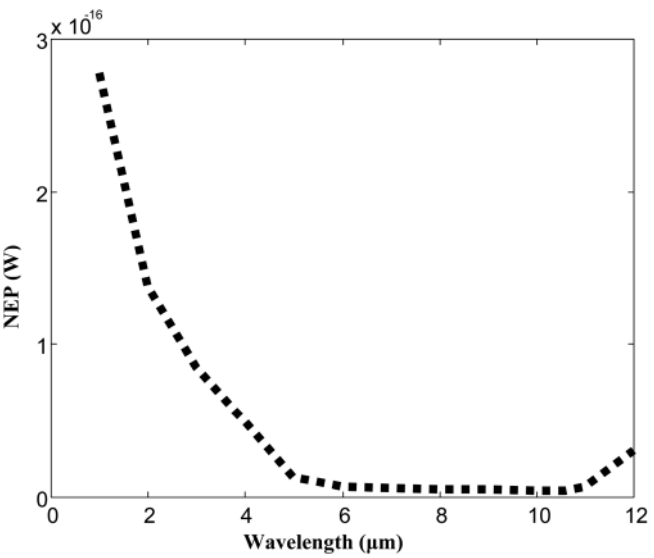

FIG. 11. Variation of noise equivalent power with wavelength of operation.

shows variation of noise equivalent power of the photodetector with wavelength of operation. We can see that the device exhibits a very low value of noise equivalent power (NEP), of the order of 1×10^{-17} W at the desired wavelength of operation 10.6 μm; NEP increases beyond the upper cutoff wavelength of the detector, 10.6 μm; and there is a drastic increase in NEP at wavelengths below 5 μm.

CONCLUSION

The potential of a P^+-$Hg_{0.69}Cd_{0.31}Te$/n-$Hg_{0.78}Cd_{0.22}Te$/CdZnTe LWIR heterojunction photodetector has been explored theoretically for free space optical communication at 10.6 μm operating at 77 K. The performance of the device has been examined by developing an analytical model for the dark current, quantum efficiency, responsivity, and detectivity, and the results obtained from the analytical model have been compared and contrasted with those obtained from ATLAS™ device simulation software from SILVACO® International. There is a very good agreement between results obtained by the analytical model and those obtained from the ATLAS simulation. The device exhibited a very low dark current of the order of 10^{-11} A, very high quantum efficiency ~80%, responsivity ~6.75 A/W, detectivity $\sim 2.25 \times 10^{11}$ $mHz^{1/2}W^{-1}$, and noise equivalent power (NEP) $\sim 1 \times 10^{-17}$ W at wavelength of operation 10.6 μm and bias voltage of 0.5 V. The usefulness of ATLAS for the proposed photodetector design has been demonstrated in this paper. While the analytical model explores various physical mechanisms that shape the device characteristics, the simulation makes use of advanced numerical techniques to extract the performance of the P^+-n photodetector structure. A more rigorous noise analysis of the detector, which accounts for various noise components arising out of the contribution of the photodetector and preamplifier, has been carried out and is reported elsewhere.[38]

ACKNOWLEDGMENTS

The author gratefully acknowledge the support of Professor P. Chakrabarti, Coordinator, Centre for Research in Microelectronics, Department of Electronics Engineering, IT-BHU, Varanasi, India, for providing the ATLAS simulation facility at Centre for Research in Microelectronics, Department of Electronics Engineering, IT-BHU, and also for his fruitful discussion and guidance during the course of this work.

[1]H. Manor and S. Arnon, Appl. Opt. **42**(21), 4285 (2003).
[2]W. D. Hu, X. S. Chen, Z. H. Ye, and W. Lu, Semicond. Sci. Technol. **25**, 045028 (2010).
[3]A. D. D. Dwivedi and P. Chakrabarti, J. Optoelectron. Adv. Mater. Rapid Commun. **4**(4), 480 (2010).
[4]A. Jozwikowska, K. Jozwikowski, J. Antoszewski, C. A. Musca, T. Nguyen, R. H. Sewell, J. M. Dell, L. Faraone, and Z. Orman, J. Appl. Phys. **98**(1), 014504 (2005).
[5]W. D. Hu, X. S. Chen, F. Yin, Z. J. Quan, Z. H. Ye, X. N. Hu, Z. F. Li, and W. Lu, J. Appl. Phys. **105**, 104502 (2009).
[6]W. D. Hu, X. S. Chen, F. Yin, Z. H. Ye, C. Lin, X. N. Hu, Z. J. Quan, Z. F. Li, and W. Lu, Opt. Quantum Electron. **40**, 1255 (2009).
[7]W. D. Hu, X. S. Chen, Z. H. Ye, C. Lin, F. Yin, and W. Lu, Opt. Quantum Electron. **41**, 699 (2009).
[8]A. D. D. Dwivedi and P. Chakrabarti, Opt. Quantum Electron. **39**, 627 (2007).
[9]Z. J. Quan, X. S. Chen, W. D. Hu, Z. H. Ye, X. N. Hu, Z. F. Li, and W. Lu, Opt. Quantum Electron. **38**, 1107 (2006).
[10]E. Bellotti and D. D. Orsogna, IEEE J. Quantum Electron. **42**, 418 (2006).
[11]Z. J. Quan, Z. F. Li, W. D. Hu, Z. H. Ye, X. N. Hu, and W. Lu, J. Appl. Phys. **100**, 084503 (2006).
[12]J. Wenus, J. Rutkowski, and A. Rogalski, IEEE Trans. Electron Devices **48**, 1326 (2001).
[13]V. Gopal and S. Gupta, IEEE Trans. Electron Devices **50**, 1220 (2003).
[14]A. Rogalski, Rep. Prog. Phys. **68**, 2267 (2005).
[15]E. Borniol, J. Baylet, J. Zanatta, S. Mibord, O. Gravrand, F. Rothan, E. Borniol, P. Castelein, J. Chamonal, M. Ravetto, and G. Destéfanis, Proc. SPIE **4820**, 491 (2003).
[16]A. S. Gilmore, J. Bangs, and A. Gerrish, J. Electron. Mater. **34**, 913 (2005).
[17]V. Gopal, S. Gupta, R. K. Bhan, R. Pal, P. K. Chaudhary, and V. Kumar, Infrared Phys. Technol. **44**, 143 (2003).
[18]V. Gopal, S. K. Singh, and R. M. Mehra, Infrared Phys. Technol. **43**, 317 (2002).
[19]A. Rogalski, Infrared Phys. Technol. **41**, 213 (2000).
[20]A. Rogalski, K. Adamiec, and J. Rutkowski, *Narrow-Gap Semiconductor Photodiode* (SPIE, Bellingham, WA, 2000).
[21]B. L. Sharma and R. K. Purohit, *Semiconductor Heterojunctions* (Pergamon Press, New York, 1974).
[22]J. Bardeen, F. J. Blatt, and L. H. Hall, in *Photoconductivity Conference*, Atlantic City, edited by R. Breackenridge, B. Russel, and E. Hahn (Wiley, New York, 1956), pp. 146–154.
[23]W. Shockley and W. T. Read, Phys. Rev. **87**, 835 (1952).
[24]R. K. Lal and P. Chakrabarti, Opt. Quantum Electron. **36**, 935 (2004).
[25]S. M. Sze, *Physics of Semiconductor Devices* (Wiley Eastern Limited, New Delhi, 1981).
[26]J. V. Gumenjuk-Sichevskaya and F. F. Sizov, Semicond. Sci. Technol. **14**, 1124 (1999).
[27]R. K. Lal, M. Jain, S. Gupta, and P. Chakrabarti, IEE Proc. Optoelectron. **150**(6), 527 (2003).
[28]Y. Tian, B. Zhang, T. Zhan, H. Jiang, and Y. Jin, IEEE Trans. Electron Devices **47**, 544 (2000).
[29]X. Y. Gong, T. Yamaguchi, H. Kan, T. Makino, T. Iida, T. Kato, and M. Kumagawa, Jpn. J. Appl. Phys. **36**, 2614 (1997).
[30]P. Chakrabarti, A. Krier, and A. F. Morgan, IEEE Trans. Electron Devices **50**, 2049 (2003).
[31]P. Capper, Properties of Narrow Gap Cadmium-Based Compounds, EMIS Data Reviews Series, No. 10 (INSPEC, The Institution of Electrical Engineers, London, 1995).
[32]M. H. Weiler, "Magnetooptical properties of $Hg_{1-x}Cd_xTe$ alloyed," in *Semiconductors and Semimetals*, Vol. 16, edited by R. K. Willardsen and A. C. Beer, pp. 119–191 (Academic Press, New York, 1981).
[33]J. Chu, Z. Mi, and D. Tang, J. Appl. Phys. **71**, 3955 (1992).
[34]J. Chu, B. Li, K. Liu, and D. Tang, J. Appl. Phys. **75**, 1234 (1994).
[35]ATLAS User's Manual Version 5.10.0.R, SILVACO International, Santa Clara, CA 95054, 2005.
[36]A. D. D. Dwivedi, A. Mittal, A. Agrawal, and P. Chakrabarti, Infrared Phys. Technol. **53**(4), 236 (2010).
[37]A. D. D. Dwivedi, J. Electron Devices **9**, 396 (2011).
[38]A. D. D. Dwivedi and P. Chakrabarti, Optoelectronics Letters, **5**(1), 21 (2009).